Available online at www.sciencedirect.com
ScienceDirect
Journal of the Mechanics and Physics of Solids 56 (2008) 815–838
JOURNAL OF THE MECHANICS AND PHYSICS OF SOLIDS
www.elsevier.com/locate/jmps

The stress concentration near a rigid line inclusion in a prestressed, elastic material. Part I. Full-field solution and asymptotics

Francesco Dal Corso, Davide Bigoni*, Massimiliano Gei

Department of Mechanical and Structural Engineering, University of Trento, via Mesiano 77, I-38050 Trento, Italy

Received 30 March 2007; received in revised form 30 June 2007; accepted 3 July 2007

Abstract

A lamellar (zero-thickness) rigid inclusion, so-called 'stiffener', is considered embedded in a uniformly prestressed (or prestrained), incompressible and orthotropic elastic sheet, subject to a homogeneous far-field deformation increment. This problem is solved under the assumption of plane strain deformation, with prestress principal directions and orthotropy axes aligned with the stiffener. A full-field solution is obtained solving the Riemann–Hilbert problem for symmetric incremental loading at infinity (while for shear deformation the stiffener leaves the ambient field unperturbed). In addition to the full-field solution, the asymptotic Mode I near-tip representation involving the corresponding incremental stress intensity factor are derived and these results are complemented with the Mode II asymptotic solution. For null prestress, the full-field stress state is shown to match correctly with photoelastic experiments performed by us (on two-part epoxy resin samples containing an aluminum lamina). Our experiments also confirm the fracture patterns for a brittle material containing a stiffener, which do not obey a hoop-stress criterion and result completely different from those found for cracks. Issues related to shear band formation and evaluation of energy release rate for a stiffener growth (or reduction) are deferred to Part II of this article.

Keywords: Stiffener; Residual stress; Fracture patterns; Photoelasticity; Experiments on materials containing inclusions

1. Introduction

Imposing large deformation to a soft, ductile metal matrix containing a thin lamellar hard phase is a well-established industrial process for the production of ultra high strength materials (Öztürk et al., 1994; Michler et al., 2004). A number of instabilities at the microscale occurs during this process and, in particular, the deformation of the soft phase has been shown to be very localized in the proximity of the stiff, thin inclusions (Öztürk et al., 1991). Localization of deformation in the form of shear bands is usually related to loss of ellipticity (of the equations governing quasi-static incremental deformation). Therefore, the availability of an analytical solution for a thin, rigid inclusion, a so-called 'stiffener', embedded in a remotely loaded,

*Corresponding author. Tel.: +39 0461 882507; fax: +39 0461 882599.
E-mail addresses: francesco.dalcorso@ing.unitn.it (F. Dal Corso), bigoni@ing.unitn.it (D. Bigoni), mgei@ing.unitn.it (M. Gei).
URL: http://www.ing.unitn.it/~bigoni/ (D. Bigoni).

0022-5096/$ - see front matter © 2007 Elsevier Ltd. All rights reserved.
doi:10.1016/j.jmps.2007.07.002

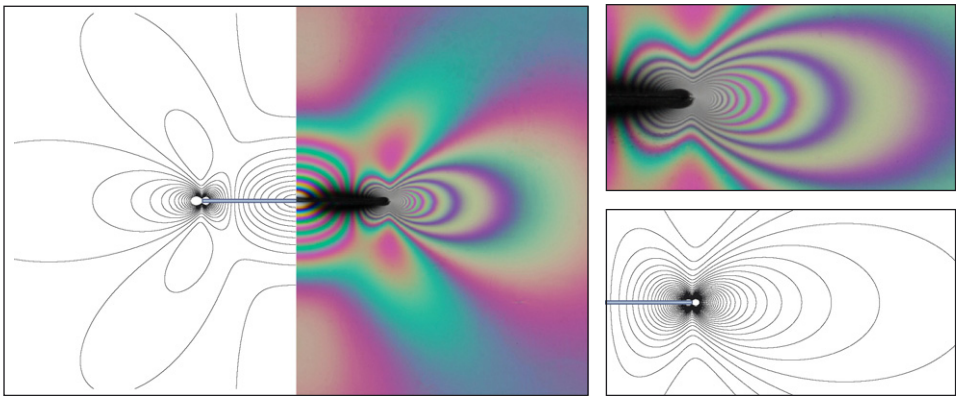

Fig. 1. Isochromatic fringe pattern obtained employing a transmission photoelastic test with polarization axes inclined at $\pm\pi/4$ with respect to the stiffener (a near-tip detail is reported right) at 0.11 MPa mean tensile loading on a (10.3 mm thick, two-component epoxy resin) sample (S1 in Appendix A) containing an (20 mm × 10.3 mm × 0.3 mm) aluminum platelet (photo taken with a Nikon D200 digital camera at the University of Trento). Photoelastic results are compared with theoretical solution in terms of in-plane principal stress difference contours plotted for an incompressible and isotropic elastic material, initially unstressed, and deformed in plane strain (see Appendix A for a full discussion).

infinite medium—in which stress and displacement fields can be obtained for an incremental perturbation superimposed upon a stress state near the boundary of ellipticity loss—is important for understanding the mechanical behaviour of the above-mentioned materials. The achievement of this solution is the main result of the present article. However, we also notice that (even for linearly elastic isotropic materials) a stiffener determines a singular solution that poses a number of questions, not arising in other situations (particularly, in the case of a crack, which induces the same singularity). In fact, it can be observed that:

- While cracks can 'naturally' exist in ordinary materials, can a stiffener—which necessarily is something artificial—be in practice introduced in a real material?
- Due to several possible discrepancies (not arising in the crack problem) between model and reality (a stiff, thin inclusion has a finite thickness and stiffness, and adhesion at the stiffener/matrix contact is necessarily imperfect), will the real stress state correspond to the elastic solution?
- Unlike cracks, stiffeners can produce a singular, non-trivial stress even when they are subject to compressive stresses or when they are pulled in uniaxial tension parallelly to them. Will a material in these cases fail due to the presence of the singularity?
- For tensile (or compressive) loading parallel (or orthogonal) to the stiffener, the material is predicted to fail through the generation of a fracture orthogonal to the stiffener at its end and not following the hoop-stress criterion valid for cracks. Will this prediction be in practice true?

Having found nothing on these issues in the literature, we have designed and realized stiffeners in a real material and produced and tested samples (details are reported in Appendix A[1]). Results of two experiments are shown in Figs. 1 and 2. In particular, the isochromatic fringe pattern recorded in a transmission photoelastic test performed with a plane polariscope is reported in Fig. 1, strikingly confirming the analytical solution for the in-plane principal stress difference contours (an incompressible, isotropic material initially unstressed has been considered).

The fracture growth sequence for tensile loading parallel to the stiffener is reported in Fig. 2, which—according to the linear elastic theory (without prestress)—develops orthogonally to the stiffener end. Therefore, our experiments provide positive answers to the questions listed above, so that the stiffener model may be considered a sound model in elasticity[2] (a systematic discussion on Mode I fracture modes at a stiffener tip is reported in Section 4).

[1]Additional experimental results are available on: http://www.ing.unitn.it/dims/laboratories/structural_modeling_photoelasticity.php.

[2]It may be worth noting that our photoelastic and failure experiments show that the hypotheses of plane strain and incompressibility do not alter results qualitatively. Regarding the former assumption, since a stiffener imposes null deformation on his surface, any sufficiently wide

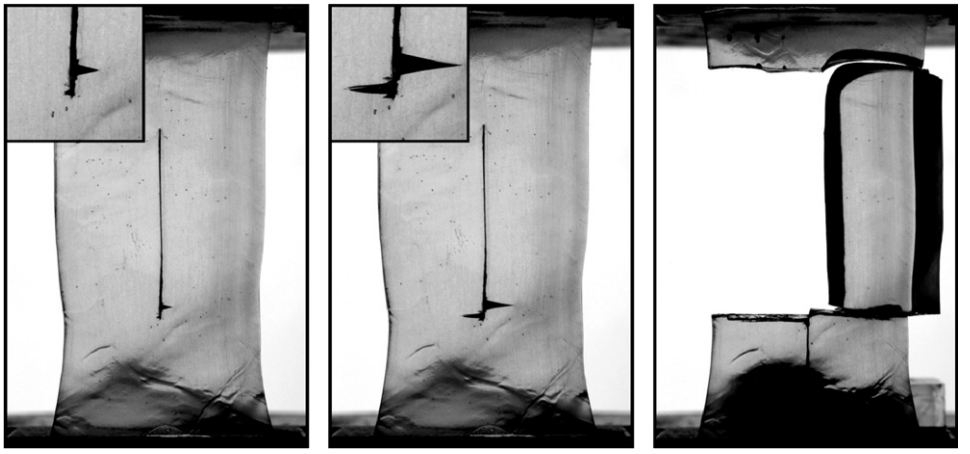

Fig. 2. Growth of two fractures at the end of an (30 mm × 10.6 mm × 0.3 mm) aluminum platelet embedded in a (10.6 mm thick, two-component epoxy resin) sample (S2 in Appendix A) under vertical tensile loading (photos taken with a Nikon D200 digital camera at the University of Trento). Both fractures have initiated horizontally (at a mean stress near to 30 MPa), where the stiffener is still attached to the resin (a detachment has developed at the end of the stiffener, due to out-of-plane contraction, see Appendix A for a full discussion).

Going back now to the main goal of the present article, a thin, rigid line inclusion is considered embedded in an infinite, incompressible, orthotropic material[3] uniformly prestressed (or prestrained), with principal stress directions aligned parallel and orthogonal to the inclusion (the formulation is given in Section 2). When a generic perturbation field is superimposed upon this state, a stress singularity is produced near the inclusion tip. The Modes I and II asymptotic fields are obtained (in Section 3) with a complex potential technique similar to that employed by Radi et al. (2002), revealing a stress singularity $\sim 1/\sqrt{r}$, as in the case when the prestress is absent. Moreover, a perturbation in the form of a uniform Eulerian strain increment field is considered at infinity. In this case, only the perturbation stress fields satisfying Mode I symmetry are non-trivial (for incremental shear deformation at infinity the stiffener leaves the fields unperturbed) and their determination represents the solution of a Riemann–Hilbert problem, which is already known in the absence of prestress for isotropic or anisotropic (compressible) elasticity (Wang et al., 1985; Ballarini, 1987; Wu, 1990; Hurtado et al., 1996; Dascalu and Homentcovschi, 1999; Homentcovschi and Dascalu, 2000; see also Koiter, 1955; Erdogan and Gupta, 1972; Atkinson, 1973 where an elastic lamellar inclusion has been considered), but has never been considered for a prestressed material.[4] This solution is provided in this paper (Section 5) within the elliptic range and it can be exploited until near the boundary of ellipticity loss, thus revealing the emergence of localized deformation patterns (an important problem deferred to Part II of this article, together with considerations of incremental energy release rate for stiffener growth). Note that our solution is strictly valid when the state of prestress upon which the modes I and II perturbations are superimposed is uniform. Obviously, such a uniform prestress state cannot result from uniform remote loading of a homogeneous material containing a stiffener. Therefore, our calculations are strictly applicable to a model problem, which describes a situation in which a uniform stress is generated, for instance, through a constrained transformation strain (such a uniform temperature variation or phase transformation of a specimen with prevented

(*footnote continued*)
platelet embedded in a material will have a state of plane strain prevailing near its centre (see also the discussion reported in Appendix A). Regarding the latter assumption, extension of our results to compressible orthotropic, incremental elasticity is straightforward and does not change qualitatively results for shear band emergence.

[3]More in detail, the material model falls within the Biot (1965) constitutive framework, which embraces Mooney–Rivlin and Ogden (1972, 1984) materials and the J_2-deformation theory of plasticity (useful in the modelling of rubber materials and for the analysis of the loading response of highly deformed metals, see Hutchinson and Neale, 1979; Hutchinson and Tvergaard, 1981).

[4]Guz and co-workers (see Guz, 1999 and references quoted therein) and Soós and co-workers (see Cristescu et al., 2004 and references quoted therein) have solved a number of problems for prestressed elastic materials, but—as far as the authors are aware—they have never considered stiffeners.

displacements at the boundary, see Li et al., 2003; Zheng et al., 2000), or in which a rigid thin layer is 'welded' subsequently to a uniform prestrain of a material. However, direct comparison of our solutions with experimental results performed by Öztürk et al. (1991) and by us (see Part II of this article) shows that our model is able to correctly predict the shear band patterns evidenced near the tip of the stiffener when the surrounding field is inhomogeneously deformed (a circumstance also confirmed by numerical solutions not reported for conciseness). Briefly, we believe that this fact is not incidental, rather it is related to the circumstance that localized deformations within shear bands dominate previously developed inhomogeneous, but small, deformation (see also the discussion on Part II of this article).

2. Governing incremental equations

Consider a two-dimensional, incompressible, elastic body, homogeneously prestressed along two orthogonal directions, x_1 and x_2, with Cauchy principal stresses denoted by σ_1 and σ_2. A zero-thickness stiffener of length $2l$ is aligned along the axis x_1 such that it occupies a segment S having extremal points of coordinates $(-l,0)$, $(l,0)$ in the system Ox_1x_2 (Fig. 3).

The incremental, orthotropic, response of the body is governed by the Biot (1965) constitutive equations (see Radi et al., 2002; Brun et al., 2003 for details), relating the increment in nominal stress $\dot{t}_{ij}$ to the incremental in-plane mean stress $\dot{p}$ and displacement gradient $v_{i,j}$ as

$$\begin{aligned} \dot{t}_{11} &= \mu(2\xi - k - \eta)v_{1,1} + \dot{p}, & \dot{t}_{22} &= \mu(2\xi + k - \eta)v_{2,2} + \dot{p}, \\ \dot{t}_{12} &= \mu[(1+k)v_{2,1} + (1-\eta)v_{1,2}], & \dot{t}_{21} &= \mu[(1-\eta)v_{2,1} + (1-k)v_{1,2}], \end{aligned} \tag{1}$$

where incompressibility requires (the usual summation convention for repeated indices is assumed)

$$v_{i,i} = 0. \tag{2}$$

In Eqs. (1), μ is the incremental shear modulus, while ξ, η, k are dimensionless constants depending on the principal components of Cauchy prestress σ_1 and σ_2 and on the incremental modulus μ_* for a shear inclined at $\pi/4$ to the principal stress axes, namely

$$\xi = \frac{\mu_*}{\mu}, \quad \eta = \frac{p}{\mu} = \frac{\sigma_1 + \sigma_2}{2\mu}, \quad k = \frac{\sigma_1 - \sigma_2}{2\mu}. \tag{3}$$

The Cauchy stress tensor and the nominal stress tensor are related through $\boldsymbol{\sigma} = J^{-1}\mathbf{F}\mathbf{t}$, where $\mathbf{F}$ is the deformation gradient and $J = \det \mathbf{F} = 1$ for incompressibility.

Obviously, the material response depends much on the choice of the specific elastic model and related potential, which dictates the dependence of incremental moduli (3) on the stretches in the current configuration. We will use two models as paradigmatic examples: the Mooney–Rivlin material and the J_2-deformation theory of plasticity, yielding quite different results (the interested reader is referred to Brun et al., 2003 for a detailed explanation of these material models).

Incremental equilibrium ($\dot{t}_{ij,i} = 0$) yields the following two equations:

$$\begin{aligned} \dot{p}_{,1} &= \mu[(1 + k - 2\xi)v_{1,11} - (1-k)v_{1,22}], \\ \dot{p}_{,2} &= \mu[(1 - k - 2\xi)v_{2,22} - (1+k)v_{2,11}], \end{aligned} \tag{4}$$

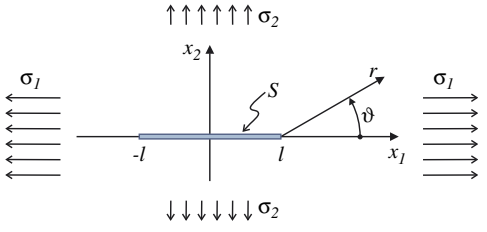

Fig. 3. Stiffener, prestressed state and reference systems.

that, together with Eq. (2), provide a system of partial differential equations for v_1, v_2 and $\dot{p}$. A *stream function* $\psi(x_1, x_2)$ with the property

$$v_1 = \psi_{,2}, \quad v_2 = -\psi_{,1}, \tag{5}$$

then satisfying Eq. (2) can be introduced, so that the elimination of $\dot{p}$ in Eq. (4) gives the fourth-order partial differential equation

$$(1+k)\psi_{,1111} + 2(2\xi - 1)\psi_{,1122} + (1-k)\psi_{,2222} = 0. \tag{6}$$

A solution of Eq. (6) can be represented in terms of the analytic function $\widehat{F}$

$$\psi(x_1, x_2) = \widehat{F}(x_1 + \Omega x_2), \tag{7}$$

where Ω is a complex constant satisfying a biquadratic equation obtained inserting representation (7) in Eq. (6). Its four roots Ω_j ($j = 1, \ldots, 4$) satisfy

$$\Omega_j^2 = \frac{1 - 2\xi + (-1)^j \sqrt{4\xi^2 - 4\xi + k^2}}{1-k}, \tag{8}$$

and are real or complex depending on the values of ξ and k. In compact form, we write $\Omega_j = \alpha_j + \mathrm{i}\beta_j$ ($j = 1, \ldots, 4$) and define the four complex variables

$$z_j = x_1 + \Omega_j x_2 = x_1 + \alpha_j x_2 + \mathrm{i}\beta_j x_2 \quad (j = 1, \ldots, 4), \tag{9}$$

where $\mathrm{i} = \sqrt{-1}$ and $\alpha_j = \mathrm{Re}[\Omega_j]$ and $\beta_j = \mathrm{Im}[\Omega_j]$.

Through Eqs. (7) and (9), the general solution of the differential equation (6) can be recast as

$$\psi(x_1, x_2) = \sum_{j=1}^{4} \widehat{F}_j(z_j). \tag{10}$$

The field quantities may be obtained by the following conditions:

- the stream function ψ must be real valued;
- the velocity field must satisfy the constraint (leaving an arbitrary rigid-body rotation of the stiffener unprescribed)

$$v_{1,1}(x_1, 0) = v_{2,11}(x_1, 0) = 0 \quad \text{if } |x_1| < l, \tag{11}$$

  on the rigid line inclusion;
- the incremental stress field must satisfy the symmetry conditions (asymptotic problem) or the condition on the incremental nominal stress (produced by prescribed Eulerian strain) at infinity (full-field problem).

2.1. Classification of regimes

The roots Ω_j, defined by Eq. (8) and changing their nature according to the values taken by parameters ξ and k, can be classified as follows.

- Four real roots in the hyperbolic regime (H) ($k^2 < 1$ and $2\xi < 1 - \sqrt{1-k^2}$),

$$\left.\begin{array}{l} \Omega_1 = \alpha_1 \\ \Omega_2 = \alpha_2 \\ \Omega_3 = -\Omega_1 \\ \Omega_4 = -\Omega_2 \end{array}\right. \quad \text{where } \left.\begin{array}{l} \alpha_1 \\ \alpha_2 \end{array}\right\} = \sqrt{\frac{1 - 2\xi \pm \sqrt{4\xi^2 - 4\xi + k^2}}{1-k}}. \tag{12}$$

- Two real and two imaginary roots in the parabolic regime (P) ($k^2>1$),

$$\left.\begin{array}{l}\Omega_1=\alpha\\ \Omega_2=\mathrm{i}\beta\\ \Omega_3=-\Omega_1\\ \Omega_4=-\Omega_2\end{array}\right. \quad \text{where} \left.\begin{array}{l}\alpha\\ \beta\end{array}\right\} = \sqrt{\frac{1-2\xi\mp \mathrm{Sign}[k]\sqrt{4\xi^2-4\xi+k^2}}{1-k}}. \tag{13}$$

- Four complex conjugate roots in the elliptic complex (EC) regime ($k^2<1$ and $1-\sqrt{1-k^2}<2\xi<1+\sqrt{1-k^2}$),

$$\left.\begin{array}{l}\Omega_1=-\alpha+\mathrm{i}\beta\\ \Omega_2=\alpha+\mathrm{i}\beta\\ \Omega_3=\overline{\Omega}_1\\ \Omega_4=\overline{\Omega}_2\end{array}\right. \quad \text{where} \left.\begin{array}{l}\alpha\\ \beta\end{array}\right\} = \sqrt{\frac{\sqrt{1-k^2}\mp(2\xi-1)}{2(1-k)}}. \tag{14}$$

- Four imaginary conjugate roots in the elliptic imaginary (EI) regime ($k^2<1$ and $2\xi>1+\sqrt{1-k^2}$),

$$\left.\begin{array}{l}\Omega_1=\mathrm{i}\beta_1\\ \Omega_2=\mathrm{i}\beta_2\\ \Omega_3=\overline{\Omega}_1\\ \Omega_4=\overline{\Omega}_2\end{array}\right. \quad \text{where} \left.\begin{array}{l}\beta_1\\ \beta_2\end{array}\right\} = \sqrt{\frac{2\xi-1\pm\sqrt{4\xi^2-4\xi+k^2}}{1-k}}. \tag{15}$$

A sketch of regime classification in the $k-\xi$ plane has been given by Radi et al. (2002, their Fig. 2).

The following analysis is restricted to the elliptic regime (the cases EC and EI are treated separately), where shear bands in terms of discontinuities of the gradient of incremental displacement are excluded.

3. Asymptotic solution of a stiffener embedded in an elastic, prestressed infinite plane

Near the tip of the rigid line inclusion the kinematic and static fields may be approximated by their asymptotic expansions. Let us focus on the tip of coordinates $(l,0)$. The complex variables z_j $(j=1,\dots,4)$ defined in Eq. (9) admit the polar representation

$$z_j = l + r_j \mathrm{e}^{\mathrm{i}\vartheta_j} \quad (j=1,\dots,4;\text{no sum on index } j), \tag{16}$$

with

$$\begin{aligned} r_j &= r\sqrt{(\cos\vartheta+\alpha_j\sin\vartheta)^2+\beta_j^2\sin^2\vartheta},\\ \tan\vartheta_j &= \frac{\beta_j\sin\vartheta}{\cos\vartheta+\alpha_j\sin\vartheta} \quad (j=1,\dots,4;\text{no sum on index } j), \end{aligned} \tag{17}$$

where r and ϑ are the polar coordinates of a generic point (Fig. 3).

In the neighbourhood of the tip $(l,0)$ the stream function can be now expressed in the power-expansion form

$$\psi(x_1,x_2) = \frac{2\dot{K}}{3\mu\sqrt{\pi}}\sum_{j=1}^{4} A_j (z_j-l)^{\gamma} = \frac{4\dot{K}}{3\mu\sqrt{\pi}}\sum_{n=1}^{2}\mathrm{Re}[A_n w_n^{\gamma}], \tag{18}$$

where the notation $w_j = z_j - l = r_j \mathrm{e}^{\mathrm{i}\vartheta_j}$ $(j=1,\dots,4)$ has been introduced. The last term is a two-term summation because $\overline{w_j^{\gamma}} = \overline{w_j}^{\gamma}$ and, as the stream function must be real-valued, the complex constants A_j satisfy the property $A_3=\overline{A}_1$ and $A_4=\overline{A}_2$. Constants A_n $(n=1,2)$ may be represented as

$$A_n = a_n + \mathrm{i}b_n \quad (n=1,2), \tag{19}$$

with a_n and b_n real constants. The parameter $\dot{K}$ plays the role of an incremental intensity factor, remains undetermined in an asymptotic analysis and will be discussed in detail later in this section.

3.1. Symmetry conditions

The asymptotic form of the relevant quantities in Modes I and II loading conditions can be obtained imposing the following symmetry conditions on the incremental displacement field:

$$\text{Mode I: } v_1(x_1,x_2)=v_1(x_1,-x_2),\quad v_2(x_1,x_2)=-v_2(x_1,-x_2), \tag{20}$$

$$\text{Mode II: } v_1(x_1,x_2)=-v_1(x_1,-x_2),\quad v_2(x_1,x_2)=v_2(x_1,-x_2). \tag{21}$$

In the next subsection, the asymptotic fields in the vicinity of the line tip for the EC regime will be derived for both Modes I and II, summarizing in Appendix B the analogous procedure for the EI regime.

3.2. Asymptotic fields in the EC regime

In the EC regime the roots Ω_j $(j=1,\dots,4)$ assume the form (14). The asymptotic expansions of the incremental quantities may be obtained by substituting the expression of the stream function $(18)_2$ in Eqs. (5), (1), and (4) (see Radi et al., 2002 for details) to yield

$$\begin{aligned}
v_1 &= \frac{4\gamma\dot{K}}{3\mu\sqrt{\pi}}\sum_{n=1}^{2}\{(-1)^n\alpha\,\mathrm{Re}[A_n w_n^{\gamma-1}]-\beta\,\mathrm{Im}[A_n w_n^{\gamma-1}]\},\\
v_2 &= -\frac{4\gamma\dot{K}}{3\mu\sqrt{\pi}}\sum_{n=1}^{2}\mathrm{Re}[A_n w_n^{\gamma-1}],\\
\dot{t}_{11} &= \frac{4\gamma\dot{K}}{3\sqrt{\pi}}(\gamma-1)\sum_{n=1}^{2}\{(-1)^n(\beta\delta+\chi\alpha)\,\mathrm{Re}[A_n w_n^{\gamma-2}]+(\alpha\delta-\chi\beta)\mathrm{Im}[A_n w_n^{\gamma-2}]\},\\
\dot{t}_{22} &= \frac{4\gamma\dot{K}}{3\sqrt{\pi}}(\gamma-1)\sum_{n=1}^{2}\{(-1)^n(\beta\delta-\chi\alpha)\,\mathrm{Re}[A_n w_n^{\gamma-2}]+(\alpha\delta+\chi\beta)\,\mathrm{Im}[A_n w_n^{\gamma-2}]\},\\
\dot{t}_{12} &= -\frac{4\gamma\dot{K}}{3\sqrt{\pi}}(\gamma-1)\sum_{n=1}^{2}\{(\chi\beta^2-\chi\alpha^2+2\alpha\beta\delta)\,\mathrm{Re}[A_n w_n^{\gamma-2}]\\
&\quad+(-1)^n(\delta\alpha^2-\delta\beta^2+2\chi\alpha\beta)\,\mathrm{Im}[A_n w_n^{\gamma-2}]\},\\
\dot{t}_{21} &= -\frac{4\gamma\dot{K}}{3\sqrt{\pi}}(\gamma-1)\sum_{n=1}^{2}\{\chi\,\mathrm{Re}[A_n w_n^{\gamma-2}]+(-1)^n\delta\,\mathrm{Im}[A_n w_n^{\gamma-2}]\},\\
\dot{p} &= \frac{4\gamma\dot{K}}{3\sqrt{\pi}}(\gamma-1)\sum_{n=1}^{2}\{(-1)^n\alpha[2(1-k)\beta^2+k]\mathrm{Re}[A_n w_n^{\gamma-2}]\\
&\quad+\beta[2(1-k)\alpha^2-k]\,\mathrm{Im}[A_n w_n^{\gamma-2}]\},
\end{aligned} \tag{22}$$

where coefficients χ,δ depend on the prestress and on the incremental moduli through the expressions

$$\chi=2\xi-\eta,\quad \delta=2(1-k)\alpha\beta=\sqrt{4\xi-4\xi^2-k^2}. \tag{23}$$

3.2.1. Mode I

Through Eq. (14) and the definition of w_j, Mode I symmetry conditions (20) write

$$v_1(w_1,w_2)=v_1(\overline{w}_2,\overline{w}_1),\quad v_2(w_1,w_2)=-v_2(\overline{w}_2,\overline{w}_1), \tag{24}$$

which imply

$$A_n=(-1)^n a+\mathrm{i}b\quad(n=1,2), \tag{25}$$

where a and b are real constants. The boundary conditions (11) on the rigid line inclusion ($\vartheta = \pi$ or, equivalently, $\vartheta_n = \pi$) lead to the following homogeneous system for the constants a and b:

$$a\alpha \cos\gamma\pi - b\beta\cos\gamma\pi = 0, \quad b\sin\gamma\pi = 0. \tag{26}$$

Non-trivial solution for a and b of system (26) exists if and only if the determinant of the associated matrix vanishes, occurring when $\alpha\sin(2\gamma\pi) = 0$. Note that α vanishes when

$$\xi = \tfrac{1}{2}\left(1 + \sqrt{1-k^2}\right), \tag{27}$$

which represents the boundary between EI and EC domains. Therefore, within the EC regime and assuming boundedness of incremental energy, we find $\gamma = \frac{3}{2}$, similarly to the stiffener problem in classical linear elasticity. For $\gamma = \frac{3}{2}$, Eq. $(26)_2$ gives $b = 0$.

The asymptotic analysis is completed by expressing each variable appearing in Eq. (22) as a product of a term depending on the radius r with that describing the angular dependence around the rigid-line tip (variable ϑ)

$$\boldsymbol{v}(r,\vartheta) = \frac{\dot{K}}{\mu}\sqrt{\frac{r}{2\pi}}\boldsymbol{\omega}(\vartheta), \quad \dot{\boldsymbol{t}}(r,\vartheta) = \frac{\dot{K}}{\sqrt{2\pi r}}\boldsymbol{\tau}(\vartheta), \quad \dot{p}(r,\vartheta) = \frac{\dot{K}}{\sqrt{2\pi r}}\rho(\vartheta). \tag{28}$$

Since the constant $\dot{K}$ remains undetermined in an asymptotic analysis, it is expedient now to introduce a normalization. For the problem of fracture, Radi et al. (2002) have defined

$$\dot{K}_{\mathrm{I}} = \lim_{r\to 0}\sqrt{2\pi r}\ \dot{t}_{22}(r,\vartheta=0), \quad \dot{K}_{\mathrm{II}} = \lim_{r\to 0}\sqrt{2\pi r}\ \dot{t}_{21}(r,\vartheta=0), \tag{29}$$

for Modes I and II incremental loading, respectively. This definition becomes unpractical in the present context. In fact, $\tau_{22}(0)$ (and $\tau_{21}(0)$ for Mode II) vanishes for certain values of prestress, indicated by a dashed curve in Fig. 4 (note that $\tau_{22}(0) = 0$—and $\tau_{21}(0) = 0$ for Mode II—even in the case when the prestress is zero).

Therefore, since $\omega_{2,2}$ (or $\omega_{2,1}$) never vanishes (under the assumption that $\alpha \neq 0$) for Mode I (or for Mode II), we follow the suggestion by Wu (1990) and introduce the definition

$$\dot{K}_{(\varepsilon)\mathrm{I}} = \lim_{r\to 0} 2\mu\sqrt{2\pi r}\ v_{2,2}(r,\vartheta=0), \quad \dot{K}_{(\varepsilon)\mathrm{II}} = \lim_{r\to 0} 2\mu\sqrt{2\pi r}\ v_{2,1}(r,\vartheta=0), \tag{30}$$

yielding for Mode I the representation

$$\boldsymbol{v}(r,\vartheta) = \frac{\dot{K}_{(\varepsilon)\mathrm{I}}}{\mu}\sqrt{\frac{r}{2\pi}}\boldsymbol{\omega}(\vartheta), \quad \dot{\boldsymbol{t}}(r,\vartheta) = \frac{\dot{K}_{(\varepsilon)\mathrm{I}}}{\sqrt{2\pi r}}\boldsymbol{\tau}(\vartheta), \quad \dot{p}(r,\vartheta) = \frac{\dot{K}_{(\varepsilon)\mathrm{I}}}{\sqrt{2\pi r}}\rho(\vartheta), \tag{31}$$

where the Mode I incremental stress intensity factor $\dot{K}_{(\varepsilon)\mathrm{I}}$ now appears. The relation between the definitions (30) of incremental stress intensity factors and the energy release rate will be obtained in Part II of this article and will be shown to be particularly convenient from a mathematical point of view.

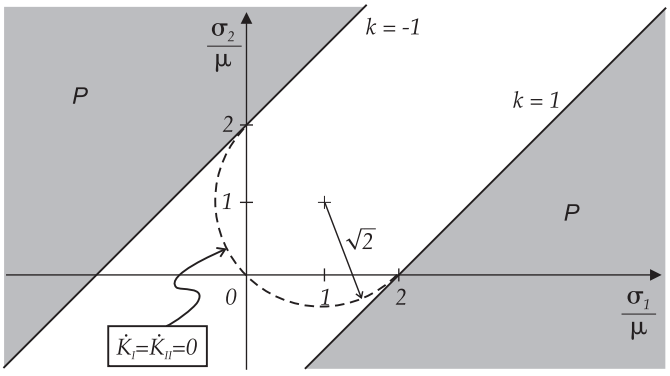

Fig. 4. Line (dashed) of points where $\dot{K}_{\mathrm{I}} = 0$ for Mode I and $\dot{K}_{\mathrm{II}} = 0$ for Mode II in the prestress plane $\sigma_1/\mu - \sigma_2/\mu$. The white zone denotes the elliptic and the hyperbolic (EI ∪ EC ∪ H) regimes, while the grey zones refer to the parabolic (P) regime.

The components of the angular functions defined in Eq. (31) for a generic Mode I symmetry assume the following analytical expressions valid for $\vartheta \in [0, \pi]$:

$$\begin{aligned}
\omega_1(\vartheta) &= 2a\sum_{n=1}^{2}[\alpha c_n(\vartheta) - (-1)^n \beta s_n(\vartheta)],\\
\omega_2(\vartheta) &= -2a\sum_{n=1}^{2}(-1)^n c_n(\vartheta),\\
\tau_{11}(\vartheta) &= a\sum_{n=1}^{2}[(\beta\delta + \chi\alpha)\hat{c}_n(\vartheta) - (-1)^n(\alpha\delta - \chi\beta)\hat{s}_n(\vartheta)],\\
\tau_{22}(\vartheta) &= a\sum_{n=1}^{2}[(\beta\delta - \chi\alpha)\hat{c}_n(\vartheta) - (-1)^n(\alpha\delta + \chi\beta)\hat{s}_n(\vartheta)],\\
\tau_{12}(\vartheta) &= -a\sum_{n=1}^{2}[(-1)^n(\chi\beta^2 - \chi\alpha^2 + 2\alpha\beta\delta)\hat{c}_n(\vartheta) - (\delta\alpha^2 - \delta\beta^2 + 2\alpha\beta\chi)\hat{s}_n(\vartheta)],\\
\tau_{21}(\vartheta) &= -a\sum_{n=1}^{2}[(-1)^n\chi\hat{c}_n(\vartheta) - \delta\hat{s}_n(\vartheta)],\\
\rho(\vartheta) &= a\sum_{n=1}^{2}\{\alpha[2(1-k)\beta^2 + k]\hat{c}_n(\vartheta) - (-1)^n\beta[2(1-k)\alpha^2 - k]\hat{s}_n(\vartheta)\},
\end{aligned} \tag{32}$$

where the following angular functions have been introduced:

$$\begin{aligned}
g_n(\vartheta) &= \sqrt{[\cos\vartheta + (-1)^n\alpha\sin\vartheta]^2 + \beta^2\sin^2\vartheta},\\
c_n(\vartheta) &= \sqrt{g_n(\vartheta) + \cos\vartheta + (-1)^n\alpha\sin\vartheta}, \quad \hat{c}_n(\vartheta) = \frac{c_n(\vartheta)}{g_n(\vartheta)},\\
s_n(\vartheta) &= \sqrt{g_n(\vartheta) - \cos\vartheta - (-1)^n\alpha\sin\vartheta}, \quad \hat{s}_n(\vartheta) = \frac{s_n(\vartheta)}{g_n(\vartheta)}.
\end{aligned} \tag{33}$$

The definition of $\dot{K}_{(\varepsilon)\mathrm{I}}$ $(30)_1$ introduces the normalization condition

$$\left.\frac{\mathrm{d}\omega_2(\vartheta)}{\mathrm{d}\vartheta}\right|_{\vartheta=0} = 2, \tag{34}$$

leading to the following expression for constant $a = -1/(4\sqrt{2}\alpha)$.

3.2.2. Mode II

Through Eq. (14) and the definition of w_j, Mode II symmetry conditions (21) write

$$v_1(w_1, w_2) = -v_1(\overline{w}_2, \overline{w}_1), \quad v_2(w_1, w_2) = v_2(\overline{w}_2, \overline{w}_1), \tag{35}$$

which imply

$$A_n = -a - (-1)^n \mathrm{i}b \quad (n = 1, 2), \tag{36}$$

being a and b real constants. The boundary conditions (11) yield the homogeneous linear problem

$$a\beta\sin\gamma\pi + b\alpha\sin\gamma\pi = 0, \quad a\cos\gamma\pi = 0, \tag{37}$$

that leads, again, to $\alpha\sin(2\gamma\pi) = 0$. For $\gamma = \frac{3}{2}$, Eq. $(37)_1$ defines a constraint on the constants a and b, namely, $b = -a\beta/\alpha$.

Analogously to Mode I, the asymptotic fields may be represented as a product between the Mode II incremental stress intensity factor $\dot{K}_{(\varepsilon)\mathrm{II}}$ (Eq. $(30)_2$) and two functions depending on r and ϑ, respectively, as

$$\boldsymbol{v}(r,\vartheta)=\frac{\dot{K}_{(\varepsilon)\mathrm{II}}}{\mu}\sqrt{\frac{r}{2\pi}}\boldsymbol{\omega}(\vartheta),\quad \dot{\boldsymbol{t}}(r,\vartheta)=\frac{\dot{K}_{(\varepsilon)\mathrm{II}}}{\sqrt{2\pi r}}\boldsymbol{\tau}(\vartheta),\quad \dot{p}(r,\vartheta)=\frac{\dot{K}_{(\varepsilon)\mathrm{II}}}{\sqrt{2\pi r}}\rho(\vartheta), \tag{38}$$

where $\boldsymbol{\omega}(\vartheta)$, $\boldsymbol{\tau}(\vartheta)$ and $\rho(\vartheta)$ assume, in the range $\vartheta\in[0,\pi]$, the form

$$\begin{aligned}
\omega_1(\vartheta)&=-2a\frac{\alpha^2+\beta^2}{\alpha}\sum_{n=1}^{2}(-1)^n c_n(\vartheta),\\
\omega_2(\vartheta)&=2a\frac{1}{\alpha}\sum_{n=1}^{2}[\alpha c_n(\vartheta)+(-1)^n\beta s_n(\vartheta)],\\
\tau_{11}(\vartheta)&=a\frac{\alpha^2+\beta^2}{\alpha}\sum_{n=1}^{2}[-(-1)^n\chi\hat{c}_n(\vartheta)+\delta\hat{s}_n(\vartheta)],\\
\tau_{22}(\vartheta)&=a\frac{\alpha^2+\beta^2}{\alpha}\sum_{n=1}^{2}[(-1)^n\chi\hat{c}_n(\vartheta)+\delta\hat{s}_n(\vartheta)],\\
\tau_{12}(\vartheta)&=-a\frac{\alpha^2+\beta^2}{\alpha}\sum_{n=1}^{2}[(\alpha\chi-\beta\delta)\hat{c}_n(\vartheta)+(-1)^n(\alpha\delta+\beta\chi)\hat{s}_n(\vartheta)],\\
\tau_{21}(\vartheta)&=-a\frac{1}{\alpha}\sum_{n=1}^{2}[-(\alpha\chi-\beta\delta)\hat{c}_n(\vartheta)+(-1)^n(\alpha\delta+\beta\chi)\hat{s}_n(\vartheta)],\\
\rho(\vartheta)&=a\frac{\alpha^2+\beta^2}{\alpha}\sum_{n=1}^{2}[-(-1)^n k\hat{c}_n(\vartheta)+\delta\hat{s}_n(\vartheta)].
\end{aligned} \tag{39}$$

The normalization condition, $\omega_2(0)=4$, now fixes the constant a to be $a=1/(4\sqrt{2})$.

4. The strange failure modes near a stiffener in a brittle material

The analysis of the near-tip asymptotic fields reveals interesting features, deserving a detailed description, confined here to Mode I loading, Eqs. (B.4). In particular, let us start with the angular distribution of Mode I asymptotic near-tip fields, represented in Fig. 5 for a Mooney–Rivlin material, $\xi=1$ at different levels of prestress $k=\{-0.4,0,0.4\}$. The values $k=\pm0.4$ are sufficiently far from the EI/P boundary, which is attained by a Mooney–Rivlin material at an infinite stretch, when $k=\pm1$. The value $k=0$ pertains to the case of the isotropic incompressible elasticity with null prestress.

The normalization (30) is used, so that the loading is given by an incremental dilatation orthogonal to the stiffener $v_{2,2}>0$ (which, due to incompressibility, is equivalent to a contraction parallel to the stiffener). We may note from the figure that the angular distribution is not affected much by prestress, except that the two nominal shear stresses separate and that the radial stress always remains negative for $k=0.4$.

Interestingly, compressive stresses dominate and, in particular, the hoop stress is always negative for $k>0$. Therefore, assuming that *the material is brittle*, *in the sense that it fails when the maximum tensile hoop stress reaches a limit value*, we note that:

- *the maximum hoop-stress criterion* (Erdogan and Sih, 1963) *does not work*;
- *failure will not occur with a fracture aligned parallel to the stiffener, even when this is subject to a Mode I loading.*

For simplicity, let us focus on the situation without prestress, $k=0$, and assume that the matrix material is brittle, therefore failing in agreement with a maximum principal stress criterion (so that obviously the following considerations will depend on these assumptions). The maximum principal stress is attained at the stiffener line ($\theta=\pi$) and is inclined at $\pi/4$ (Fig. 6, left). In this case, the failure mode is not easy to be

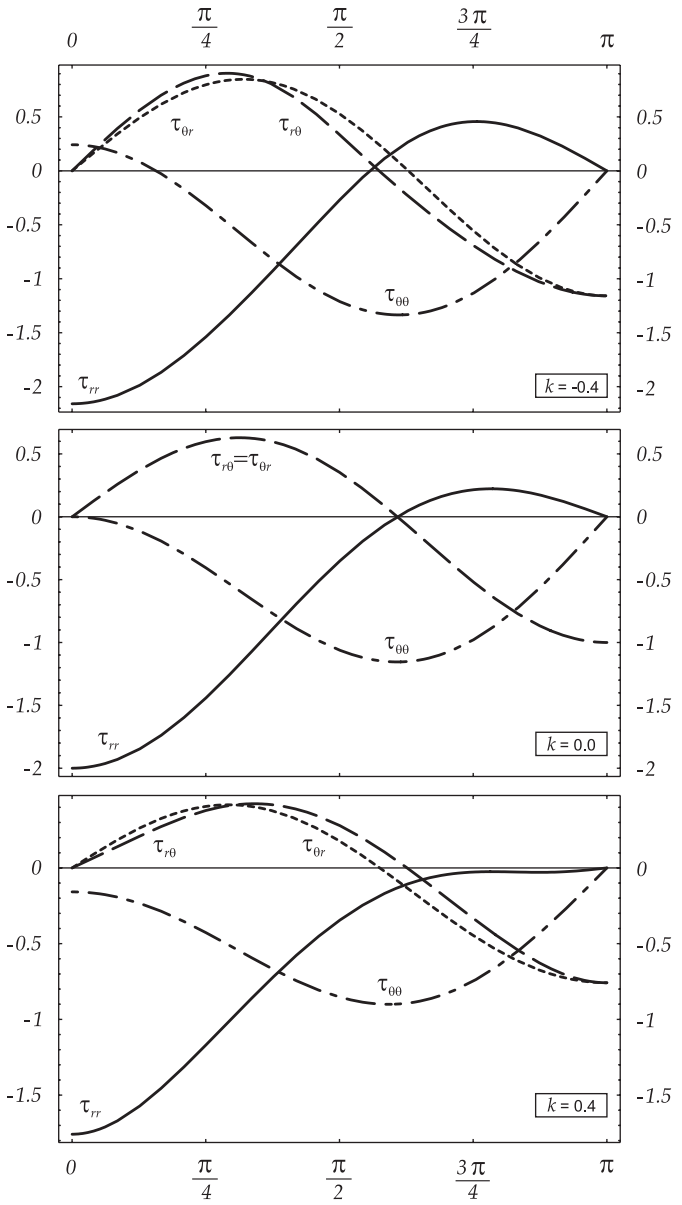

Fig. 5. Angular representation of asymptotic Mode I stress field near the tip of a stiffener in an incompressible, elastic Mooney–Rivlin material at different levels of prestress k.

envisaged. Our interpretation is that:

a crack starts on the surface of the inclusion inclined at $\pi/4$ (orthogonal to the principal, near-tip tensile direction) and immediately after the stiffener delaminates and the crack propagates under opening mode (orthogonally to the loading direction);

this situation has been in fact observed in one of our experiments, see Appendix A and Fig. 8.

If now a dilatation parallel to the stiffener is considered, $v_{1,1}>0$ (Fig. 6, right), all signs of the stresses reverse in the graphs reported in Fig. 5 and we may understand that

failure occurs due to the maximum radial stress,

which is the maximum near-tip principal stress.

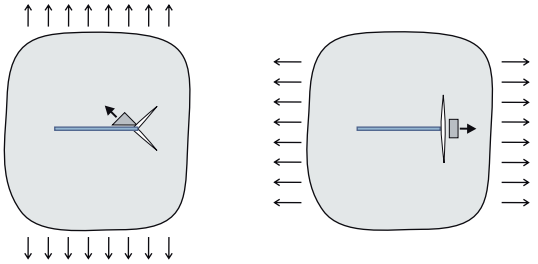

Fig. 6. Sketch of the predicted fracture modes for a stiffener embedded in an isotropic, not prestressed, brittle matrix (where cracks develop orthogonally to the maximum tensile stress), subject to orthogonal (left) and parallel (right) dilatation. Compare the failure mode shown on the left with Fig. 8, that shown on the right with Figs. 2 and 7.

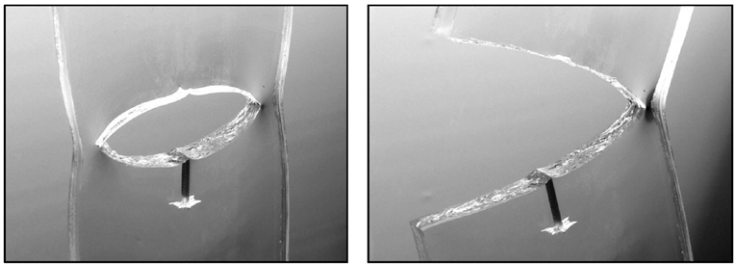

Fig. 7. Progressive fracture of sample S1 subject to a tensile load directed parallel to the inclusion (photo taken at the University of Trento with a Panasonic DMC-FZ5 digital camera). Note that there are two fractures, one at the upper tip and another, much less developed, at the lower tip of the aluminum lamina.

The fracture patterns sketched in Fig. 6 have been confirmed by three experiments. In particular, fractures similar to that shown in Fig. 6 (right) have been found in samples S2, S1, reported in Figs. 2 and 7, respectively. Fractures similar to that shown in Fig. 6 (left) have been found in sample S4, see Fig. 8.

Until now we have investigated a brittle matrix material, so that a moderate prestress has been considered and its effects have been shown to be relatively limited. However, ductile materials can be subject to severe prestress and its effects become dramatic when the prestress parameter approaches the value for ellipticity loss and in this case near-tip localized deformations emerge, a situation that completely changes the failure modes (and will be analysed in detail in Part II of the present article).

5. Full-field solution of a stiffener embedded in an elastic, prestressed infinite plane

The full-field solution is obtained for the problem where a uniformly prestressed, infinite plane containing a stiffener of length $2l$ (aligned parallel to the principal stress directions) is subject to remote incremental loading, with prescribed incremental displacement gradient. In particular, the non-null far-field stress components $\dot{t}_{11}^{(\infty)}$ and $\dot{t}_{22}^{(\infty)}$ are prescribed (respectively, along directions x_1 and x_2, Fig. 3), corresponding to a type of Mode I loading. Mode II will not be considered since a stiffener aligned parallel to axis x_1 does not perturb a uniform incremental shear parallel to the axes (a fact that can be intuitively appreciated thinking about a shearing deformation of a deck of cards and its associated strain ellipses).

Using superposition, the solution to the above-problem can be attained in the following two steps:

1. the unperturbed problem (denoted with the apex '∞'), where the homogeneous, infinite domain (without inclusions) is subject to the homogeneous incremental displacement gradient $v_{1,1}^{(\infty)} = -v_{2,2}^{(\infty)}$ and $v_{1,2}^{(\infty)} = v_{2,1}^{(\infty)} = 0$;
2. the non-trivial problem (denoted with the apex '$\circ$') where the incremental displacement gradient is prescribed to assume—along the stiffener line S—opposite values than those calculated at step 1.

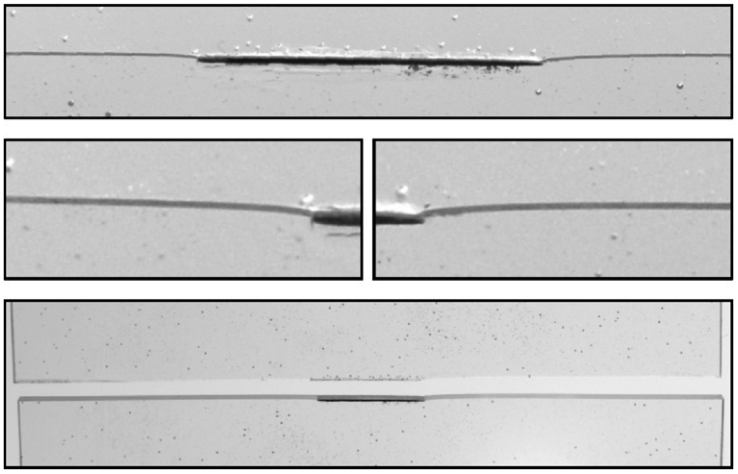

Fig. 8. Fracture mode of sample S4 subject to a tensile load orthogonal to the inclusion. The aluminum lamina is visible in the upper part, while the two near-tip details are shown in the central part. A 'post-mortem' view of the fracture is shown in the lower part, where the two pieces of the sample have been separated. Note the initial inclinations (approximately $\pi/4$) of the fractures near the aluminum lamina tips (photos taken at the University of Trento with a Nikon D200 digital camera).

For both problems, the solution is known once the associated stream function is obtained, as kinematic and static quantities can be easily derived from it.

5.1. Unperturbed problem

The incremental nominal stress $\dot{t}_{ij}^{(\infty)}$ is homogeneous in the unperturbed problem, with principal components matching exactly the applied far-field incremental displacement gradient. Taking $2\xi \neq \eta$ for simplicity, the constitutive equations (1) allow us to relate the displacement gradient and the incremental pressure in the form

$$\begin{aligned} &v_{1,1}^{(\infty)} = -v_{2,2}^{(\infty)} = \frac{\dot{t}_{11}^{(\infty)} - \dot{t}_{22}^{(\infty)}}{2\mu(2\xi - \eta)}, \quad \dot{t}_{12}^{(\infty)} = \dot{t}_{21}^{(\infty)} = 0, \\ &\dot{p}^{(\infty)} = \frac{\dot{t}_{11}^{(\infty)}(2\xi + k - \eta) + \dot{t}_{22}^{(\infty)}(2\xi - k - \eta)}{2(2\xi - \eta)}, \end{aligned} \tag{40}$$

so that we can equivalently prescribe remote incremental nominal stresses instead of incremental displacement gradient components.

Fulfilment of Eq. $(40)_1$ requires a stream function $\psi^{(\infty)}$ depending only on z_1 and z_2, which in the EI regime takes the form

$$\psi^{(\infty)}(z_1, z_2) = -\frac{v_{2,2}^{(\infty)}}{4\beta_1\beta_2}\,\mathrm{Im}[\beta_2 z_1^2 + \beta_1 z_2^2], \tag{41}$$

while in the EC regime

$$\psi^{(\infty)}(z_1, z_2) = \frac{v_{2,2}^{(\infty)}}{4(\alpha^2 + \beta^2)}\{\alpha\,\mathrm{Re}[z_1^2 - z_2^2] - \beta\,\mathrm{Im}[z_1^2 + z_2^2]\}. \tag{42}$$

The trivial cases when $\dot{t}_{11}^{(\infty)} = \dot{t}_{22}^{(\infty)} = \dot{t}^{(\infty)}$ and $2\xi = \eta$ are not considered here for conciseness.

5.2. Non-trivial problem

The constraint introduced by the stiffener imposes the fulfilment of conditions (11). Therefore, the displacement gradient components $v_{1,1}$ and $v_{2,1}$, of opposite sign to that imposed in the unperturbed problem,

are applied on the line representing the lamellar inclusion, namely

$$\left(-v^{(\circ)}_{1,1}(x_1,0)=\right)v^{(\circ)}_{2,2}(x_1,0)=-v^{(\infty)}_{2,2}\quad\text{if } |x_1|<l,$$
$$v^{(\circ)}_{2,1}(x_1,0)=-v^{(\infty)}_{2,1}(x_1,0)=0,\quad \forall\, x_1\in\mathbb{R}. \tag{43}$$

Note that $v_{2,11}=0$ is now equivalent to $v_{2,1}=0$, due to Mode I symmetry.

The solution is derived separately for the two EC and EI regimes (beginning with EC). We introduce functions $F_1(z_1)$ and $F_2(z_2)$, so that the stream function $\psi^{(\circ)}$ is given by

$$\psi^{(\circ)}(z_1,z_2)=\mathrm{Re}\left[\sum_{j=1}^{2}F_j(z_j)\right]. \tag{44}$$

Consequently, the displacement gradient becomes

$$v^{(\circ)}_{1,1}(z_1,z_2)=\mathrm{Re}\left[\sum_{j=1}^{2}\Omega_j F_j''(z_j)\right],\quad v^{(\circ)}_{2,1}(z_1,z_2)=-\mathrm{Re}\left[\sum_{j=1}^{2}F_j''(z_j)\right]. \tag{45}$$

The effects of the applied boundary conditions on the inclusion segment decay and vanish at infinity, so that, from Eq. (45) we get

$$\lim_{|z_j|\to+\infty}F_j''(z_j)=0\quad(j=1,2). \tag{46}$$

Moreover, Eqs. $(43)_2$ and $(45)_2$ provide

$$v^{(\circ)}_{2,1}(x_1,0)=-\frac{F_1''^{+}(x_1)-F_1''^{-}(x_1)}{2}-\frac{F_2''^{+}(x_1)-F_2''^{-}(x_1)}{2}=0,\quad \forall\, x_1\in\mathbb{R}, \tag{47}$$

(where apices + and − denote the upper and lower stiffener surface, respectively) which yields the key property

$$(F_1''(x_1)+F_2''(x_1))^{+}=(F_1''(x_1)+F_2''(x_1))^{-},\quad \forall\, x_1\in\mathbb{R}. \tag{48}$$

Condition (48) implies that the function $F_1''(x_1)+F_2''(x_1)$ is continuous across the branch cut, so that it results analytic in the whole Ox_1x_2 plane, and, assuming also boundedness, it results constant from Liouville's theorem. Such a constant is zero since at infinity the function must be zero, see Eq. (46). As a conclusion, we obtain

$$F_1''(x_1)=-F_2''(x_1),\quad \forall x_1\in\mathbb{R}. \tag{49}$$

The set of equation (49), plus Eqs. (15), (14), and (45) allow us to represent function $v^{(\circ)}_{1,1}$ on S in the form

$$v^{(\circ)}_{1,1}(x_1,0)=-2\alpha\,\mathrm{Re}[F_1''(x_1)]+(\beta_1-\beta_2)\mathrm{Re}[\mathrm{i}F_1''(x_1)], \tag{50}$$

so that condition $(43)_1$ takes the form

$$-2\alpha\,\mathrm{Re}[F_1''(x_1)]+(\beta_1-\beta_2)\mathrm{Re}[\mathrm{i}F_1''(x_1)]=v^{(\infty)}_{2,2}\quad\text{if } |x_1|<l. \tag{51}$$

5.2.1. EC regime

In the EC regime, $\beta_1=\beta_2$, so that Eq. (51) simplifies to

$$-2\alpha\,\mathrm{Re}[F_1''(x_1)]=v^{(\infty)}_{2,2}\quad\text{if } |x_1|<l. \tag{52}$$

The following Riemann–Hilbert problem can be formulated for function $F_1''(z)$ on the rectilinear segment S, i.e.

$$F_1''^{+}(x_1)+F_1''^{-}(x_1)=-\frac{v^{(\infty)}_{2,2}}{\alpha}\quad\text{if } |x_1|<l, \tag{53}$$

whose solution is given by Muskhelishvili (1953, Section 110) in the form

$$F_1''(z_1) = -\frac{v_{2,2}^{(\infty)}}{2\alpha\sqrt{z_1^2 - l^2}}\left[\frac{1}{2\pi \mathrm{i}}\int_{-l}^{l}\frac{\sqrt{t^2 - l^2}}{t - z_1}\mathrm{d}t + P(z_1)\right], \tag{54}$$

where $P(z_1)$ is a polynomial that must be zero for the condition (46). The solution is (Carloni et al., 2002)

$$F_1''(z_1) = -\frac{v_{2,2}^{(\infty)}}{2\alpha}\left(1 - \frac{z_1}{\sqrt{z_1^2 - l^2}}\right), \tag{55}$$

and through Eq. (49)

$$F_2''(z_2) = \frac{v_{2,2}^{(\infty)}}{2\alpha}\left(1 - \frac{z_2}{\sqrt{z_2^2 - l^2}}\right). \tag{56}$$

By integration, Eq. $(44)_1$ provides $\psi^{(\circ)}$ within the EC regime. In this regime, the stream function ψ writes

$$\begin{aligned}\psi = \psi^{(\circ)} + \psi^{(\infty)} = & -\frac{v_{2,2}^{(\infty)}}{4\alpha}\left\{\mathrm{Re}\left[\beta^2\frac{z_1^2 - z_2^2}{\alpha^2 + \beta^2} - z_1\sqrt{z_1^2 - l^2} + z_2\sqrt{z_2^2 - l^2}\right.\right.\\ & \left.\left. + l^2\ln\left(\frac{z_1 + \sqrt{z_1^2 - l^2}}{z_2 + \sqrt{z_2^2 - l^2}}\right)\right] + \mathrm{Im}\left[\alpha\beta\frac{z_1^2 + z_2^2}{\alpha^2 + \beta^2}\right]\right\}.\end{aligned} \tag{57}$$

The incremental displacement field and its gradient can be calculated from Eqs. (5) and are reported in Appendix C. Eqs. (1) and (4) provide the incremental nominal stress field in the form

$$\begin{aligned}\dot{p} - \dot{p}^{(\infty)} = & -\frac{\mu v_{2,2}^{(\infty)}}{2\alpha}\left\{-\alpha[2(1-k)\beta^2 + k]\,\mathrm{Re}\left[2 - \frac{z_1}{\sqrt{z_1^2 - l^2}} - \frac{z_2}{\sqrt{z_2^2 - l^2}}\right]\right.\\ & \left. -\beta[2(1-k)\alpha^2 - k]\,\mathrm{Im}\left[\frac{z_1}{\sqrt{z_1^2 - l^2}} - \frac{z_2}{\sqrt{z_2^2 - l^2}}\right]\right\},\end{aligned}$$

$$\begin{aligned}\dot{t}_{11} - \dot{p}^{(\infty)} = & -\frac{\mu v_{2,2}^{(\infty)}}{2\alpha}\left\{(\beta\delta + \chi\alpha)\,\mathrm{Re}\left[\frac{z_1}{\sqrt{z_1^2 - l^2}} + \frac{z_2}{\sqrt{z_2^2 - l^2}}\right]\right.\\ & \left. -(\alpha\delta - \chi\beta)\,\mathrm{Im}\left[\frac{z_1}{\sqrt{z_1^2 - l^2}} - \frac{z_2}{\sqrt{z_2^2 - l^2}}\right] - 2\alpha[2(1-k)\beta^2 + k]\right\},\end{aligned}$$

$$\begin{aligned}\dot{t}_{22} - \dot{p}^{(\infty)} = & -\frac{\mu v_{2,2}^{(\infty)}}{2\alpha}\left\{(\beta\delta - \chi\alpha)\,\mathrm{Re}\left[\frac{z_1}{\sqrt{z_1^2 - l^2}} + \frac{z_2}{\sqrt{z_2^2 - l^2}}\right]\right.\\ & \left. -(\alpha\delta + \chi\beta)\,\mathrm{Im}\left[\frac{z_1}{\sqrt{z_1^2 - l^2}} - \frac{z_2}{\sqrt{z_2^2 - l^2}}\right] - 2\alpha[2(1-k)\beta^2 + k]\right\},\end{aligned}$$

$$\dot{t}_{12} = -\frac{\mu v_{2,2}^{(\infty)}}{2\alpha}\left\{(\chi\beta^2 - \chi\alpha^2 + 2\alpha\beta\delta)\,\mathrm{Re}\left[\frac{z_1}{\sqrt{z_1^2-l^2}} - \frac{z_2}{\sqrt{z_2^2-l^2}}\right]\right.$$
$$\left. -(\delta\alpha^2 - \delta\beta^2 + 2\alpha\beta\chi)\,\mathrm{Im}\left[\frac{z_1}{\sqrt{z_1^2-l^2}} + \frac{z_2}{\sqrt{z_2^2-l^2}}\right]\right\},$$

$$\dot{t}_{21} = -\frac{\mu v_{2,2}^{(\infty)}}{2\alpha}\left\{\chi\,\mathrm{Re}\left[\frac{z_1}{\sqrt{z_1^2-l^2}} - \frac{z_2}{\sqrt{z_2^2-l^2}}\right] - \delta\,\mathrm{Im}\left[\frac{z_1}{\sqrt{z_1^2-l^2}} + \frac{z_2}{\sqrt{z_2^2-l^2}}\right]\right\}, \tag{58}$$

where $\dot{p}^{(\infty)}$ is given by Eq. $(40)_3$ and the parameters χ and δ are defined by Eqs. (23).

Employing the definition of $\dot{K}_{(\varepsilon)\mathrm{I}}$ given by Eq. $(30)_1$, we obtain

$$\dot{K}_{(\varepsilon)\mathrm{I}} = 2\mu v_{2,2}^{(\infty)}\sqrt{\pi l}, \tag{59}$$

while, if we use the definition $(29)_1$ of incremental stress intensity factor (instead of definition $(30)_1$), we get

$$\dot{K}_{\mathrm{I}} = -\mu v_{2,2}^{(\infty)}\sqrt{\pi l}\left[\sqrt{1-k^2} - 1 + \eta\right]. \tag{60}$$

Note that, due to the different normalizations, both the definitions (59) and (60) differ from that employed by Cristescu et al. (2004) for cracks and by Ballarini (1990) for stiffeners in the infinitesimal theory. Interestingly, the incremental stress intensity factor (59) [differently from the other definition (60)] is independent of the prestress, so that it coincides with the corresponding stress intensity factor of the infinitesimal theory.

We note that the full-field solution (58) matches the asymptotic one (28), (32) when both z_1 and z_2 approach l. Moreover, all terms of the type $z_n/\sqrt{z_n^2-l^2}$ $(n=1,2)$ become leading order contributions, behaving as $1/\sqrt{r}$ near the line tip.

5.2.2. EI regime

In the EI regime, $\alpha = 0$, so that Eq. (51) becomes

$$(\beta_1 - \beta_2)\mathrm{Re}[\mathrm{i}F_1''(x_1)] = v_{2,2}^{(\infty)} \quad \text{if } |x_1|<l, \tag{61}$$

providing the following Riemann–Hilbert problem in terms of $F_1''(z)$ on S

$$F_1''^{+}(x_1) + F_1''^{-}(x_1) = -\mathrm{i}\frac{2v_{2,2}^{(\infty)}}{\beta_1 - \beta_2} \quad \text{if } |x_1|<l. \tag{62}$$

The solution of Eq. (62) corresponds to

$$F_1''(z_1) = -\mathrm{i}\frac{v_{2,2}^{(\infty)}}{\beta_1 - \beta_2}\left(1 - \frac{z_1}{\sqrt{z_1^2-l^2}}\right), \tag{63}$$

while Eq. (49) provides

$$F_2''(z_2) = \mathrm{i}\frac{v_{2,2}^{(\infty)}}{\beta_1 - \beta_2}\left(1 - \frac{z_2}{\sqrt{z_2^2-l^2}}\right). \tag{64}$$

Analogously to the EC regime, the stream function $\psi^{(\circ)}$ can be obtained integrating equations (63) and (64) and employing Eq. $(44)_2$. This gives

$$\psi = \psi^{(\infty)} + \psi^{(\circ)} = -\frac{v_{2,2}^{(\infty)}}{2(\beta_1-\beta_2)}\,\mathrm{Im}\left[(\beta_1+\beta_2)\frac{\beta_1 z_2^2-\beta_2 z_1^2}{2\beta_1\beta_2}+z_1\sqrt{z_1^2-l^2}\right.$$
$$\left.-z_2\sqrt{z_2^2-l^2}+l^2\ln\left(\frac{z_2+\sqrt{z_2^2-l^2}}{z_1+\sqrt{z_1^2-l^2}}\right)\right]. \tag{65}$$

The incremental displacement field and its gradient are reported in Appendix C. Eqs. (1) and (4) lead to the incremental nominal stress, whose components can be expressed in terms of parameters ε_n, χ_n, and δ_n $(n=1,2)$ (see Eq. (B.2)) as

$$\dot{p}-\dot{p}^{(\infty)} = -\frac{\mu v_{2,2}^{(\infty)}}{\beta_1-\beta_2}\,\mathrm{Re}\left[\delta_1\beta_1\left(1-\frac{z_1}{\sqrt{z_1^2-l^2}}\right)-\delta_2\beta_2\left(1-\frac{z_2}{\sqrt{z_2^2-l^2}}\right)\right],$$

$$\dot{t}_{11}-\dot{p}^{(\infty)} = -\frac{\mu v_{2,2}^{(\infty)}}{\beta_1-\beta_2}\,\mathrm{Re}\left[\delta_1\beta_1-\delta_2\beta_2+\varepsilon_1\beta_1\frac{z_1}{\sqrt{z_1^2-l^2}}-\varepsilon_2\beta_2\frac{z_2}{\sqrt{z_2^2-l^2}}\right],$$

$$\dot{t}_{22}-\dot{p}^{(\infty)} = -\frac{\mu v_{2,2}^{(\infty)}}{\beta_1-\beta_2}\,\mathrm{Re}\left[\delta_1\beta_1-\delta_2\beta_2-\chi_1\beta_1\frac{z_1}{\sqrt{z_1^2-l^2}}+\chi_2\beta_2\frac{z_2}{\sqrt{z_2^2-l^2}}\right],$$

$$\dot{t}_{12} = \frac{\mu v_{2,2}^{(\infty)}}{\beta_1-\beta_2}\,\mathrm{Im}\left[\chi_1\beta_1^2\frac{z_1}{\sqrt{z_1^2-l^2}}-\chi_2\beta_2^2\frac{z_2}{\sqrt{z_2^2-l^2}}\right],$$

$$\dot{t}_{21} = \frac{\mu v_{2,2}^{(\infty)}}{\beta_1-\beta_2}\,\mathrm{Im}\left[\varepsilon_1\frac{z_1}{\sqrt{z_1^2-l^2}}-\varepsilon_2\frac{z_2}{\sqrt{z_2^2-l^2}}\right]. \tag{66}$$

The incremental stress intensity factor $\dot{K}_{(\varepsilon)\mathrm{I}}$ can be readily computed using Eq. $(30)_1$ to yield, for the EI regime, the same expression, Eq. (59), obtained for the EC regime. If we use the definition $(29)_1$ of incremental stress intensity factor instead of definition $(30)_1$, we again obtain Eq. (60), which therefore results also valid within the EI regime.

We conclude this section showing results relative to the stress fields near a stiffener as functions of the prestress (entering the formulation through dimensionless parameters η and k), for a Mooney–Rivlin material, $\xi=1$. In particular, level sets of the in-plane principal Cauchy stress increments difference, $\dot{\sigma}_1-\dot{\sigma}_2$, have been reported in Fig. 1 for null prestress, to compare with the photoelastic results. Further results with prestress levels ($\eta=k$ has been taken) up to near the elliptic boundary (EI/P) are reported in Fig. 9.

We may note from the figure that the incremental stress fields are strongly affected by the prestress (in a way which has been, in part, confirmed by our experiments, see Appendix A), so that near the EI/P boundary ($k=\pm 0.985$) localized deformations become visible, an issue that will be addressed in detail in Part II of this article.

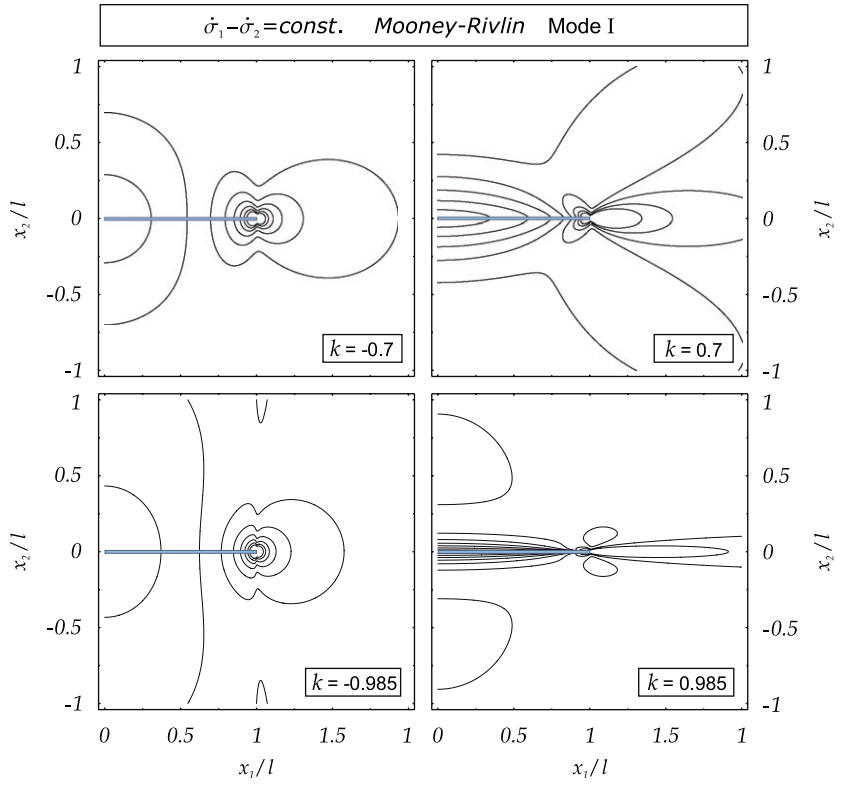

Fig. 9. Level sets of in-plane principal Cauchy stress increments difference, $\dot{\sigma}_1 - \dot{\sigma}_2$, at four prestress levels.

6. Conclusions

Asymptotic near-tip, Mode I and II fields, and a Mode I full-field solution have been obtained in this article for a thin, rigid line inclusion (a stiffener) embedded in an infinite, incompressible and orthotropic elastic medium, homogeneously prestressed and prestrained, subject to incremental non-uniform stress.

The solutions evidence interesting features even when the prestress is null, such as the fact that the material may not fail following the maximum hoop-stress criterion typical of fracture mechanics. Rather, for tensile deformations aligned parallel to the stiffener, a crack forms orthogonally to the maximum radial stress (which is aligned parallel to the stiffener so that the fracture is orthogonal to it), while for a tensile loading orthogonal to the inclusion the failure mode corresponds to a crack inclined of $\pi/4$ that nucleates on the inclusion surface and promotes delamination of the lamina and global Mode I fracture of the specimen. All these features have been confirmed by photoelastic and fracture experiments on two-component epoxy resin specimen.

The obtained solutions show that all incremental fields result to be strongly influenced by the prestress, opening the possibility of investigation of shear band nucleation and growth. Although limited to the assumption that the prestress is uniform, our analyses, presented in Part II of this paper, show that the stress/deformation incremental fields at shear band formation are similar to available experimental results.

Acknowledgements

We thank Prof. A. Pegoretti (University of Trento) for useful discussions. Resin samples have been manufactured by G. Noselli, who is gratefully acknowledged. Experiments have been conducted with the kind assistance of Mr. M. Scandella, partially at the Teaching Laboratory for Physical Modeling of Structures and Photoelasticity, managed by D.B., and partially at the Materials and Structural Testing Laboratory, managed by Prof. R. Zandonini. Financial support of MIUR-PRIN 2005 (prot. 2005085973) is gratefully acknowledged.

Appendix A. Experiments on two-component epoxy resin specimens embedding an aluminum thin platelet

A commercial two-part epoxy resin (Crystal Resin® by Gedeo, 305 Avenue du pic de Bretagne, 13420 Gemenos, France), commonly used for producing highly transparent non-yellowing casts has been employed to produce an elastic material enclosing a thin rigid lamina, to be used with transmission photoelasticity. Samples made with this resin have been de-moulded after 12 h and tested after at least one week. To realize the stiffener, we have used a 0.3 mm thick aluminum sheet, which its superficial rugosity has been improved to enhance adhesion, using a fine (P 180) sandpaper. Seven samples have been produced, five of which are shown in Fig. 10.

The square 100 mm × 100 mm × 18 mm sample (S3 in Fig. 10) has a 44 mm × 18 mm × 0.3 mm aluminum platelet embedded and has been produced following the supplier's instructions, namely, mixing one part of hardener B with two parts of resin A. When solid, after 10 days, the sample has been cut to obtain parallel edges and finally polished.

The thick rectangular 195 mm × 94.3 mm × 10.3 mm sample (S1) has a 20 mm × 10.3 mm × 0.3 mm aluminum platelet embedded and has been produced by mixing one part of hardener B with one part of resin A. In this way, a very soft material (deformed 40% longitudinally under a 0.196 MPa uniaxial mean stress at failure) has been obtained by direct casting, without any polishing.

All the other samples have been produced by mixing one part of hardener B with 2.25 parts of resin A.

The dog-bone shaped sample (S2), of thickness equal to 10.6 mm and transverse width of 39.5 mm, contains a 30 mm × 10.6 mm × 0.3 mm aluminum platelet. This sample has been cut from a circular disk sample of 115 mm diameter and finally polished.

The two rectangular 340 mm × 100 mm × 3.2 mm samples (S4, S5) contain a 15 mm × 3.2 mm × 0.3 mm aluminum platelet (parallel to the long sides in one sample and orthogonal in the other) and have been obtained by direct casting into a mould, without any further treatment.

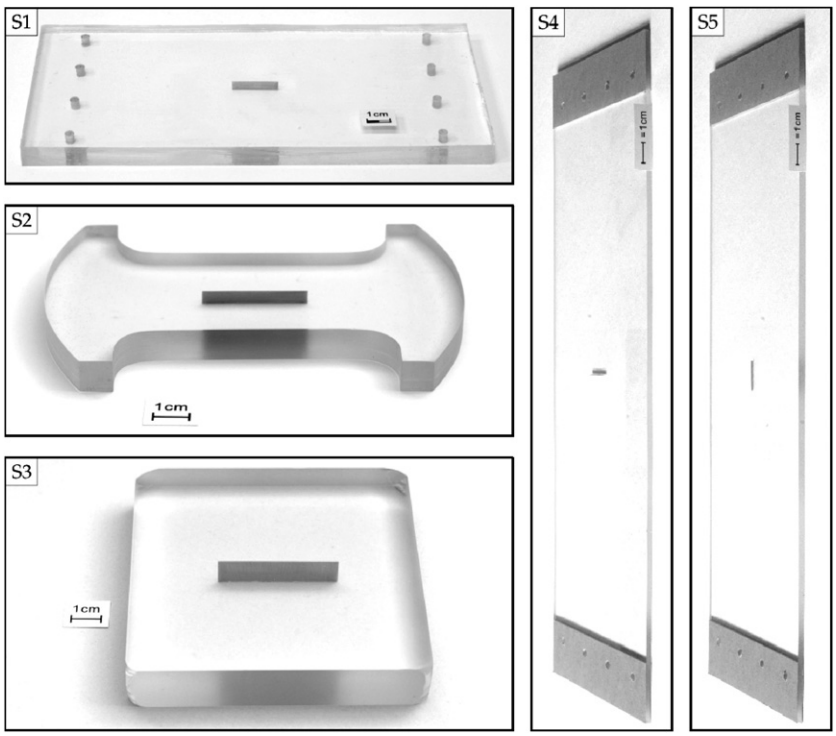

Fig. 10. The two-component epoxy resin samples with lamellar (aluminum) inclusions used in our tests. A rectangular thick sample (S1), a dog-bone shaped sample (S2), a square sample (S3), two rectangular thin samples (S4, S5) are shown (all photos have been taken with a Nikon D200 digital camera at the University of Trento).

The sample S3 has been tested under compression orthogonal to the long edge of the stiffener by imposing a vertical displacement, obtained at constant velocity of 0.1 mm/min (a Galdabini PMA 10 universal testing machine has been used). After a photoelastic investigation of the stress state has been conducted at low stress, we have tried to break the sample in compression, to investigate cracking. The material has revealed a remarkable ductile behaviour and the sample suffered an out-of-plane buckling. Therefore, the test was stopped after a large strain had occurred and before the final rupture. Interestingly, strain localization near the edges of the stiffener emerged and was made visible by reflected bright light used to illuminate the sample. One of the photos taken to reveal localization is included in Part II of this article.

The dog-bone shaped sample (S2) has been tested under tensile stress parallel to the long edge of the stiffener, by imposing a vertical displacement, obtained at constant velocity of 0.1 mm/min (a Galdabini PMA 10 universal testing machine has been used). Photoelastic investigation has been performed up to near failure stress. The sample failed at a mean stress near 36 MPa. Before failure, an out-of-plane delamination started near the lower edge of the stiffener, due to Poisson effect. Subsequently, two nearly simultaneous fractures started to grow horizontally and perpendicularly to the stiffener (Fig. 2). Initial propagation was slow, so that a few minutes elapsed from when a first fracture was visible and the photo on the left in Fig. 2 was taken (so that 30 camera shots were manually taken when a fracture was already visible, before the photo on the left in Fig. 2 was taken). About a minute elapsed and 13 camera shots were taken between the photos shown on the left and on the centre were taken. No photos were taken between those shown centrally and on the right in Fig. 2.

The three rectangular samples (S1, S4, S5) have been loaded through the imposition of dead loadings, with tensile stresses parallel to the long sides. By means of a plane polariscope, a photoelastic investigation was performed on these samples at small stress (near 4 MPa for S4 and S5, and 11 kPa for S1) giving the best quality photos, approximately identical for the three tests (Fig. 11). In particular, the isochromatic fringe patterns shown in Fig. 1 have been obtained on the soft, 10.3 mm thick rectangular sample (S1). Additional results are reported in Fig. 11, where, in particular, photos reported on the left and central have been taken on sample (S1), while the photo reported on the right has been taken on the 3.2 mm thick sample (S5).

In general, we note that plane strain deformation prevails near the stiffener, while plane stress dominates at a sufficient distance from it, particularly in samples S1 and S2. The solution for a stiffener in plane stress and plane strain isotropic (compressible) elasticity can be derived taking the limit of null semi-axes ratio for the solution of a rigid elliptical inclusion in an infinite elastic sheet reported by Muskhelishvili (1953). This solution provides contour plots of the in-plane principal stress difference qualitatively similar to the plane strain case and also both solutions do not depend much on Poisson's ratio. This explains the very good match between the theoretical results—referred to plane strain incompressible material—and the experiments shown in Fig. 1.

Although the rectangular samples provided the best photoelastic results, these analyses have been performed on all samples and always gave similar results. At very high stress, near failure under tensile stress for the dog-bone shaped specimen, the shape of the photoelastic contours evidenced details which might be better interpreted with our results for a prestressed material. However, since we had only a few of these data, we decided not to report them.

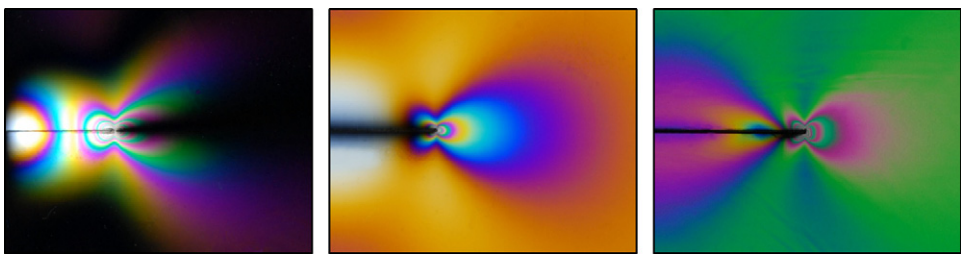

Fig. 11. Isochromatic fringe patterns captured in the photoelastic tests. Left: sample S1 at 51 kPa tensile mean stress (parallel to the stiffener); centre: sample S1 at 11 kPa tensile mean stress (parallel to the stiffener); right: sample S5 at 4.3 MPa tensile mean stress (orthogonal to the stiffener). In the left-hand side picture the axes of polarization are parallel and orthogonal to the stiffener, while these are rotated of $\pi/4$ clockwise with respect to the other two.

Appendix B. Asymptotic fields in the EI regime

Roots Ω_j ($j=1,\dots,4$) take the form (15) in the EI regime. The asymptotic expansions of the incremental quantities may be obtained by substituting the expression of the stream function $(18)_2$ in Eqs. (5), (1), and (4) (see also Radi et al., 2002) to yield

$$
\begin{aligned}
v_1 &= -\frac{4\gamma\dot{K}}{3\mu\sqrt{\pi}}\sum_{n=1}^{2}\beta_n \operatorname{Im}[A_n w_n^{\gamma-1}],\\
v_2 &= -\frac{4\gamma\dot{K}}{3\mu\sqrt{\pi}}\sum_{n=1}^{2} \operatorname{Re}[A_n w_n^{\gamma-1}],\\
\dot{t}_{11} &= -\frac{4\gamma\dot{K}}{3\sqrt{\pi}}(\gamma-1)\sum_{n=1}^{2}\varepsilon_n\beta_n \operatorname{Im}[A_n w_n^{\gamma-2}],\\
\dot{t}_{22} &= \frac{4\gamma\dot{K}}{3\sqrt{\pi}}(\gamma-1)\sum_{n=1}^{2}\chi_n\beta_n \operatorname{Im}[A_n w_n^{\gamma-2}],\\
\dot{t}_{12} &= -\frac{4\gamma\dot{K}}{3\sqrt{\pi}}(\gamma-1)\sum_{n=1}^{2}\chi_n\beta_n^2 \operatorname{Re}[A_n w_n^{\gamma-2}],\\
\dot{t}_{21} &= -\frac{4\gamma\dot{K}}{3\sqrt{\pi}}(\gamma-1)\sum_{n=1}^{2}\varepsilon_n \operatorname{Re}[A_n w_n^{\gamma-2}],\\
\dot{p} &= \frac{4\gamma\dot{K}}{3\sqrt{\pi}}(\gamma-1)\sum_{n=1}^{2}\delta_n\beta_n \operatorname{Im}[A_n w_n^{\gamma-2}],
\end{aligned}
\tag{B.1}
$$

where

$$
\begin{aligned}
&\varepsilon_n = 1-\eta+(1-k)\beta_n^2, \quad \chi_n = 4\xi-1-\eta-(1-k)\beta_n^2,\\
&\delta_n = 2\xi-1-k-(1-k)\beta_n^2 \quad (n=1,2).
\end{aligned}
\tag{B.2}
$$

B.1. Mode I

Through Eq. (15) and the definition of w_j, Mode I symmetry conditions (20) write

$$
v_1(w_1,w_2) = v_1(\overline{w}_1,\overline{w}_2), \quad v_2(w_1,w_2) = -v_2(\overline{w}_1,\overline{w}_2),
\tag{B.3}
$$

which imply $a_1=a_2=0$, so that $A_n = \mathrm{i}b_n$, where $n=1,2$.

The boundary conditions (11), applied for $\vartheta_n=\pi$, provide a homogeneous system, which (for $\beta_1\neq\beta_2$) admits a non-trivial solution if and only if γ is $\frac{3}{2}$. Note that the condition $\beta_1\neq\beta_2$ corresponds to Eq. (27), which sets the boundary between the two Elliptic regimes. For $\gamma=\frac{3}{2}$, the relation $b_1+b_2=0$ is obtained.

The components of the angular functions defined by Eqs. (31) for a generic Mode I take the following analytic expressions, valid for $\vartheta\in[0,\pi]$,

$$
\omega_1(\vartheta) = -2\sum_{n=1}^{2} b_n\beta_n\sqrt{g_n(\vartheta)+\cos\vartheta},
$$

$$\omega_2(\vartheta) = 2\sum_{n=1}^{2} b_n \sqrt{g_n(\vartheta) - \cos\vartheta},$$

$$\tau_{11}(\vartheta) = -\sum_{n=1}^{2} b_n \varepsilon_n \beta_n \sqrt{g_n(\vartheta) + \cos\vartheta}/g_n(\vartheta),$$

$$\tau_{22}(\vartheta) = \sum_{n=1}^{2} b_n \chi_n \beta_n \sqrt{g_n(\vartheta) + \cos\vartheta}/g_n(\vartheta),$$

$$\tau_{12}(\vartheta) = -\sum_{n=1}^{2} b_n \chi_n \beta_n^2 \sqrt{g_n(\vartheta) - \cos\vartheta}/g_n(\vartheta),$$

$$\tau_{21}(\vartheta) = -\sum_{n=1}^{2} b_n \varepsilon_n \sqrt{g_n(\vartheta) - \cos\vartheta}/g_n(\vartheta),$$

$$\rho(\vartheta) = \sum_{n=1}^{2} b_n \delta_n \beta_n \sqrt{g_n(\vartheta) + \cos\vartheta}/g_n(\vartheta), \tag{B.4}$$

where

$$g_n(\vartheta) = \sqrt{\cos^2\vartheta + \beta_n^2 \sin^2\vartheta}. \tag{B.5}$$

The normalization condition (34) provides b_1 and b_2 as

$$b_n = \frac{1}{2\sqrt{2}(\beta_n - \beta_m)} \quad (n, m = 1, 2,\ m \neq n), \tag{B.6}$$

where the equalities $\varepsilon_n = \chi_m$ $(n, m = 1, 2,\ m \neq n)$, obtained from Eqs. (B.2), have been used.

B.2. Mode II

Through Eqs. (15) and the definition of w_j, Mode II symmetry conditions Eqs. (21) write

$$v_1(w_1, w_2) = -v_1(\overline{w}_1, \overline{w}_2), \quad v_2(w_1, w_2) = v_2(\overline{w}_1, \overline{w}_2), \tag{B.7}$$

that imply $b_1 = b_2 = 0$, and, as a consequence, $A_n = a_n$, where $n = 1, 2$. The boundary conditions provide a homogeneous system which admits non-trivial solution for $\gamma = \frac{3}{2}$; the same system defines the constraint

$$a_1\beta_1 + a_2\beta_2 = 0. \tag{B.8}$$

The functions defined by Eqs. (38), valid for $\vartheta \in [0, \pi]$, now become

$$\omega_1(\vartheta) = -2\sum_{n=1}^{2} a_n \beta_n \sqrt{g_n(\vartheta) - \cos\vartheta},$$

$$\omega_2(\vartheta) = -2\sum_{n=1}^{2} a_n \sqrt{g_n(\vartheta) + \cos\vartheta},$$

$$\tau_{11}(\vartheta) = \sum_{n=1}^{2} a_n \varepsilon_n \beta_n \sqrt{g_n(\vartheta) - \cos\vartheta}/g_n(\vartheta),$$

$$\tau_{22}(\vartheta) = -\sum_{n=1}^{2} a_n \chi_n \beta_n \sqrt{g_n(\vartheta) - \cos\vartheta}/g_n(\vartheta),$$

$$\tau_{12}(\vartheta) = -\sum_{n=1}^{2} a_n \chi_n \beta_n^2 \sqrt{g_n(\vartheta) + \cos\vartheta}/g_n(\vartheta),$$

$$\tau_{21}(\vartheta) = -\sum_{n=1}^{2} a_n \varepsilon_n \sqrt{g_n(\vartheta) + \cos\vartheta}/g_n(\vartheta),$$

$$\rho(\vartheta) = -\sum_{n=1}^{2} a_n \delta_n \beta_n \sqrt{g_n(\vartheta) - \cos\vartheta}/g_n(\vartheta). \tag{B.9}$$

From the normalization condition $\omega_2(0) = 4$ we obtain the following condition for the constants a_1 and a_2:

$$a_n = \frac{\beta_m}{2\sqrt{2}(\beta_n - \beta_m)} \quad (n, m = 1, 2,\ m \neq n). \tag{B.10}$$

Appendix C. Kinematical fields for the full-field solution

In the EC regime, incremental displacements and its gradient are

$$v_1 = -\frac{v_{2,2}^{(\infty)}}{2\alpha}\left\{\alpha\,\mathrm{Re}\left[\sqrt{z_1^2 - l^2} + \sqrt{z_2^2 - l^2}\right] - \beta\,\mathrm{Im}\left[z_1 - z_2 - \left(\sqrt{z_1^2 - l^2} - \sqrt{z_2^2 - l^2}\right)\right]\right\},$$

$$v_2 = \frac{v_{2,2}^{(\infty)}}{2\alpha}\left\{\mathrm{Re}\left[\beta^2 \frac{z_1 - z_2}{\alpha^2 + \beta^2} - \left(\sqrt{z_1^2 - l^2} - \sqrt{z_2^2 - l^2}\right)\right] + \alpha\beta\,\mathrm{Im}\left[\frac{z_1 + z_2}{\alpha^2 + \beta^2}\right]\right\},$$

$$v_{1,1} = -\frac{v_{2,2}^{(\infty)}}{2\alpha}\left\{\alpha\,\mathrm{Re}\left[\frac{z_1}{\sqrt{z_1^2 - l^2}} + \frac{z_2}{\sqrt{z_2^2 - l^2}}\right] + \beta\,\mathrm{Im}\left[\frac{z_1}{\sqrt{z_1^2 - l^2}} - \frac{z_2}{\sqrt{z_2^2 - l^2}}\right]\right\} = -v_{2,2},$$

$$v_{1,2} = \frac{v_{2,2}^{(\infty)}}{2\alpha}\left\{(\alpha^2 - \beta^2)\mathrm{Re}\left[\frac{z_1}{\sqrt{z_1^2 - l^2}} - \frac{z_2}{\sqrt{z_2^2 - l^2}}\right] + 2\alpha\beta\,\mathrm{Im}\left[\frac{z_1}{\sqrt{z_1^2 - l^2}} + \frac{z_2}{\sqrt{z_2^2 - l^2}}\right]\right\},$$

$$v_{2,1} = -\frac{v_{2,2}^{(\infty)}}{2\alpha}\mathrm{Re}\left[\frac{z_1}{\sqrt{z_1^2 - l^2}} - \frac{z_2}{\sqrt{z_2^2 - l^2}}\right], \tag{C.1}$$

while in the EI regime

$$v_1 = -\frac{v_{2,2}^{(\infty)}}{\beta_1 - \beta_2}\mathrm{Re}\left[(\beta_1 + \beta_2)\frac{z_2 - z_1}{2} + \beta_1\sqrt{z_1^2 - l^2} - \beta_2\sqrt{z_2^2 - l^2}\right],$$

$$v_2 = \frac{v_{2,2}^{(\infty)}}{\beta_1 - \beta_2}\mathrm{Im}\left[(\beta_1 + \beta_2)\frac{\beta_1 z_2 - \beta_2 z_1}{2\beta_1\beta_2} + \sqrt{z_1^2 - l^2} - \sqrt{z_2^2 - l^2}\right],$$

$$v_{1,1} = -\frac{v_{2,2}^{(\infty)}}{\beta_1 - \beta_2}\,\mathrm{Re}\left[\beta_1 \frac{z_1}{\sqrt{z_1^2 - l^2}} - \beta_2 \frac{z_2}{\sqrt{z_2^2 - l^2}}\right] = -v_{2,2},$$

$$v_{1,2} = \frac{v_{2,2}^{(\infty)}}{\beta_1 - \beta_2}\,\mathrm{Im}\left[\beta_1^2 \frac{z_1}{\sqrt{z_1^2 - l^2}} - \beta_2^2 \frac{z_2}{\sqrt{z_2^2 - l^2}}\right],$$

$$v_{2,1} = \frac{v_{2,2}^{(\infty)}}{\beta_1 - \beta_2}\,\mathrm{Im}\left[\frac{z_1}{\sqrt{z_1^2 - l^2}} - \frac{z_2}{\sqrt{z_2^2 - l^2}}\right]. \tag{C.2}$$

References

Atkinson, C., 1973. Some ribbon-like inclusion problems. Int. J. Eng. Sci. 11, 243–266.

Ballarini, R., 1987. An integral-equation approach for rigid line inhomogeneity problems. Int. J. Fract. 33, R23–R26.

Ballarini, R., 1990. A rigid line inclusion at a bimaterial interface. Eng. Fract. Mech. 37, 1–5.

Biot, M.A., 1965. Mechanics of Incremental Deformations. Wiley, New York.

Brun, M., Capuani, D., Bigoni, D., 2003. A boundary element technique for incremental, nonlinear elasticity. Part I: Formulation. Comput. Methods Appl. Mech. Eng. 192, 2461–2479.

Carloni, C., Piva, A., Viola, E., 2002. An alternative complex variable formulation for an inclined crack in an orthotropic medium. Eng. Fract. Mech. 70, 2033–2058.

Cristescu, N.D., Craciun, E.M., Soós, E., 2004. Mechanics of Elastic Composites. Chapman & Hall, CRC, Boca Raton.

Dascalu, C., Homentcovschi, D., 1999. Uniform asymptotic solutions for lamellar inhomogeneities in anisotropic elastic solids. SIAM J. Appl. Math. 60, 18–42.

Erdogan, F., Gupta, G., 1972. Stresses near a flat inclusion in bonded dissimilar materials. Int. J. Solids Struct. 8, 533–547.

Erdogan, F., Sih, G.C., 1963. On the crack extension in plates under plane loading and transverse shear. J. Basic Eng. 85, 519–527.

Guz, A.N., 1999. Fundamentals of the Three-dimensional Theory of Stability of Deformable Bodies. Springer, Berlin.

Homentcovschi, D., Dascalu, C., 2000. Uniform asymptotic solutions for lamellar inhomogeneities in plane elasticity. J. Mech. Phys. Solids 48, 153–173.

Hurtado, J.A., Dundurs, J., Mura, T., 1996. Lamellar inhomogeneities in a uniform stress field. J. Mech. Phys. Solids 44, 1–21.

Hutchinson, J.W., Neale, K.W., 1979. Finite strain J_2—deformation theory. In: Carlson, D.E., Shield, R.T. (Eds.), Proceedings of the IUTAM Symposium on Finite Elasticity. Martinus Nijhoff, The Hague, Boston, London, pp. 237–247.

Hutchinson, J.W., Tvergaard, V., 1981. Shear band formation in plane strain. Int. J. Solids Struct. 17, 451–470.

Koiter, W.T., 1955. On the diffusion of load from a stiffener into a sheet. Q. J. Mech. Appl. Math. VIII, 164–178.

Li, Y., Cui, L.S., Xu, H.B., Yang, D.Z., 2003. Constrained phase-transformation of a TiNi shape-memory alloy. Metall. Mater. Trans. A 34, 219–223.

Michler, G.H., Adhikari, R., Henning, S., 2004. Micromechanical properties in lamellar heterophase polymer systems. J. Mater. Sci. 39, 3281–3292.

Muskhelishvili, N.I., 1953. Some Basic Problems of the Mathematical Theory of Elasticity. P. Nordhoff Ltd., Groningen.

Ogden, R.W., 1972. Large deformation isotropic elasticity: on the correlation of theory and experiment for incompressible rubberlike solids. Proc. R. Soc. London A 326, 565–583.

Ogden, R.W., 1984. Non-linear Elastic Deformations. Ellis Horwood, Chichester.

Öztürk, T., Poole, W.J., Embury, J.D., 1991. The deformation of Cu–W laminates. Mater. Sci. Eng. A 148, 175–178.

Öztürk, T., Mirmesdagh, J., Ediz, T., 1994. Strain partitioning and plastic flow in some metal/metal laminates. Mater. Sci. Eng. A 175, 125–129.

Radi, E., Bigoni, D., Capuani, D., 2002. Effects of prestress on crack-tip fields in elastic incompressible solids. Int. J. Solids Struct. 39, 3971–3996.

Wang, Z.Y., Zhang, H.T., Chou, Y.T., 1985. Characteristics of the elastic field of a rigid line inhomogeneity. J. Appl. Mech. 52, 818–822.

Wu, K.C., 1990. Line inclusions at anisotropic bimaterial interface. Mech. Mater. 10, 173–182.

Zheng, Y.J., Cui, L.S., Zhu, D., Yang, D.Z., 2000. The constrained phase transformation of prestrained TiNi fibers embedded in metal matrix smart composite. Mat. Lett. 43, 91–96.